

Repository of the Max Delbrück Center for Molecular Medicine (MDC)
in the Helmholtz Association

<http://edoc.mdc-berlin.de/15935>

Lysosomal dysfunction caused by cellular accumulation of silica nanoparticles

Schuetz, I. and Lopez-Hernandez, T. and Gao, Q. and Puchkov, D. and Jabs, S. and Nordmeyer, D. and Schmutde, M. and Ruehl, E. and Graf, C.M. and Haucke, V.

This is a copy of the original article.

This research was originally published in *Journal of Biological Chemistry*. Schuetz, I. and Lopez-Hernandez, T. and Gao, Q. and Puchkov, D. and Jabs, S. and Nordmeyer, D. and Schmutde, M. and Ruehl, E. and Graf, C.M. and Haucke, V. Lysosomal dysfunction caused by cellular accumulation of silica nanoparticles. *J Biol Chem.* 2016; 291: 14170-14184. © 2016 by The American Society for Biochemistry and Molecular Biology, Inc.

Journal of Biological Chemistry
2016 JUL01 ; 291(27): 14170-14184
Doi: [10.1074/jbc.M115.710947](https://doi.org/10.1074/jbc.M115.710947)

Publisher: [American Society for Biochemistry and Molecular Biology](http://www.asbmb.org/)

Lysosomal Dysfunction Caused by Cellular Accumulation of Silica Nanoparticles*

Received for publication, December 16, 2015, and in revised form, May 10, 2016. Published, JBC Papers in Press, May 11, 2016, DOI 10.1074/jbc.M115.710947

Irene Schütz[‡], Tania Lopez-Hernandez[‡], Qi Gao[§], Dmytro Puchkov[‡], Sabrina Jabs^{‡¶}, Daniel Nordmeyer[§], Madlen Schumde[§], Eckart Rühl[§], Christina M. Graf[§], and Volker Hauke^{‡§¶}

From the [‡]Leibniz-Institut für Molekulare Pharmakologie (FMP), Robert-Rössle-Strasse 10, 13125 Berlin, Germany, [§]Institute of Chemistry and Biochemistry, Freie Universität Berlin, 14195 Berlin, Germany, and [¶]Max-Delbrück-Center for Molecular Medicine (MDC), Robert-Rössle-Strasse 10, 13125 Berlin, Germany

Nanoparticles (NPs) are widely used as components of drugs or cosmetics and hold great promise for biomedicine, yet their effects on cell physiology remain poorly understood. Here we demonstrate that clathrin-independent dynamin 2-mediated caveolar uptake of surface-functionalized silica nanoparticles (SiNPs) impairs cell viability due to lysosomal dysfunction. We show that internalized SiNPs accumulate in lysosomes resulting in inhibition of autophagy-mediated protein turnover and impaired degradation of internalized epidermal growth factor, whereas endosomal recycling proceeds unperturbed. This phenotype is caused by perturbed delivery of cargo via autophagosomes and late endosomes to SiNP-filled cathepsin B/L-containing lysosomes rather than elevated lysosomal pH or altered mTOR activity. Given the importance of autophagy and lysosomal protein degradation for cellular proteostasis and clearance of aggregated proteins, these results raise the question of beneficial use of NPs in biomedicine and beyond.

Nanoparticles (NPs)² are widely used as components of drugs or cosmetics and hold great promise as tools in biomedicine to improve the detection and treatment of diseases (1). For example, nanoparticle technology has enabled improvements in cancer treatment, ranging from improved efficacy of drug delivery (2) to enhanced immunogenicity of cancer vaccines (3). Moreover, NPs are used as biosensors and biomarkers (4, 5) or for DNA/drug delivery (6). Hence, it is necessary to understand the mechanisms of interaction of NPs with living cells and tissues to assess the biological consequences associated with their application in biomedicine (7). At present, the risks associated

with the biomedical application of NPs at the cellular and organismic levels remain incompletely understood (1). Among the phenotypic changes reported to be associated with the biomedical application of NPs are cellular stress responses (*i.e.* redox imbalance, oxidative stress), DNA damage, and altered gene expression (8, 9). Which of these phenotypes can be considered a direct consequence of cellular NP association or uptake and the underlying molecular mechanisms have remained in many cases unknown.

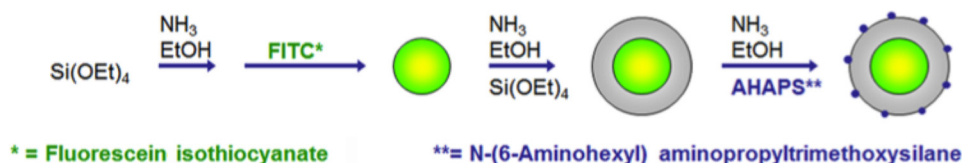
Upon cellular application, NPs initially interact with the plasma membrane, often followed by their internalization into the cell interior (10–12) via clathrin-dependent as well as clathrin-independent endocytosis routes (*i.e.* via caveolae), which may require the membrane-severing GTPase dynamin (13, 14). Due to the questionable specificity of many commonly used pharmacological tools toward these pathways (15) the precise mechanisms of cellular uptake of NPs often have remained elusive. After cell entry NPs are delivered to the endolysosomal system (16), where they may accumulate. Lysosomes play essential roles in cell physiology ranging from the degradation of malfunctioning or aggregated proteins (*e.g.* via autophagy) or lipids to nutrient signaling and cellular growth control (17). For example, internalized growth factors such as EGF are sorted to late endosomes (18), which fuse with lysosomes to deliver their intraluminal content for degradation (19). It is thus conceivable that the cellular uptake and accumulation of NPs profoundly impacts on the function of the endolysosomal system and thereby on cell physiology.

Here we have investigated the mechanisms of uptake and the intracellular trafficking itinerary of silica (SiO₂) NPs (SiNPs) in human cervix carcinoma (HeLa) cells. We demonstrate that SiNPs are internalized largely via clathrin-independent endocytosis involving dynamin 2-dependent caveolar uptake followed by their targeting to and accumulation within lysosomes. We further show that intralysosomal accumulation of SiNPs severely perturbs autophagy-mediated protein turnover and degradation of internalized epidermal growth factor due to impaired cargo delivery via autophagosomes or late multivesicular endosomes to SiNP-filled lysosomes. Consistent with these results we show that lysosomal SiNP accumulation reduces the metabolic activity of cells although it does not induce cell death due to apoptosis or necrotic cell lysis. Our results raise the question of beneficial use of NPs in biomedicine and beyond.

* This work was supported by grants from the Deutsche Forschungsgemeinschaft (DFG) (SFB 765/TP B04, C05, SPP1313/NANO-SELECT). The authors declare that they have no conflicts of interest with the contents of this article.

¹ To whom correspondence should be addressed. Tel.: 49-30-94793101; Fax: 49-30-94793109; E-mail: hauke@fmp-berlin.de.

² The abbreviations used are: NP, nanoparticle; SiNP, silica nanoparticle modified with AHAPS; AHAPS, *N*-(6-aminoethyl)-aminopropyltrimethoxysilane; EEA1, early endosome-associated antigen 1; EGFR, EGF receptor; LAMP1, lysosome-associated membrane protein 1; Tf, transferrin; LC3, microtubule-associated protein 1 light chain 3; Baf A1, bafilomycin A1; MTT, 3-[4,5-dimethylthiazol-2-yl] 2,5-diphenyl-tetrazolium bromide; p62/SQSTM1, polyubiquitin-binding protein of 62 kDa; M6PR, mannose 6-phosphate receptor; CD63, member of the tetraspanin family and a marker for late endosomes; AP-1, clathrin assembly protein 1; OGD, OR Green488 coupled to 10-kDa dextran; ULK1, UNC-51-like kinase 1; p70 S6K, mitogen-activated protein kinase of 70 kDa that phosphorylates ribosomal S6 protein; RFP, red fluorescence protein.



SCHEME 1. Scheme illustrating the synthesis of AHAPS-functionalized SiNPs using the microemulsion and Stöber technique (see "Experimental Procedures").

Results

To address the mechanism of cellular uptake and the physiological consequence of NP accumulation in mammalian cells we prepared SiNPs covalently labeled with FITC by modified microemulsion synthesis (20). The resulting dye-labeled spheres were used as cores for the subsequent seeded growth of a silica shell of 3-nm thickness based on the Stöber method (21). The surface of FITC-labeled SiNPs was modified by amino functionalization with *N*-(6-aminohexyl)-aminopropyltrimethoxysilane (AHAPS), resulting in the covalent introduction of positively charged amino groups (Scheme 1) that facilitate cellular uptake and counteract aggregation of SiNPs (22). The resulting AHAPS-functionalized SiNPs were homogeneously sized spheres with an average diameter of 75 ± 2 nm and a zeta potential of 51 ± 1 mV in ethanol and of 119 ± 2 nm and a zeta potential of 25 ± 1 mV in water (Fig. 1A, Table 1). AHAPS-modified SiNPs showed excellent colloidal stability in ethanol and in cell culture media.

To study the mechanism of SiNP uptake, cultured HeLa human cervix carcinoma cells were incubated for 4 h at 37 °C with FITC-labeled SiNPs, washed, and fixed. Analysis by confocal spinning disc microscopy revealed the accumulation of SiNPs in spherical intracellular organelles enriched in the perinuclear area. To unravel the mechanism of SiNP uptake, cells were treated with small interfering (si) RNAs to deplete them of endogenous clathrin heavy chain, a key essential component of clathrin-mediated endocytosis, flotillin 1, an integral membrane protein thought to contribute to clathrin-independent fluid-phase endocytosis via the CLIC/GEEC pathway (23, 24), or of caveolin, the main structural component of caveolae that undergoes dynamin-mediated fission (25). RNA interference resulted in the efficient and specific down-regulation of the corresponding target proteins by 85–90% (Fig. 1B). SiNP endocytosis was greatly reduced in HeLa cells depleted of caveolin 1 (using either smart pool siRNAs or a distinct single siRNA) or of dynamin 2. Knockdown of flotillin 1 led a small although statistically significant reduction in SiNP uptake, whereas SiNP endocytosis proceeded unperturbed in the absence of clathrin. Thus, AHAPS-modified SiNPs enter HeLa cells primarily via dynamin 2-mediated caveolar endocytosis (Fig. 1, C and D) independent of clathrin.

Internalized SiNPs displayed a punctuate distribution with some enrichment in the perinuclear area, suggestive of their accumulation within intracellular organelles. Intracellular SiNPs colocalized with CD63 and LAMP1, transmembrane proteins that partition between late endosomes and lysosomes (26), but not with early endosomes containing early endosomal antigen 1 (EEA1) (Fig. 2, A and B). Limited colocalization was observed with the clathrin adaptor AP-1 (assembly protein 1) and with the mannose 6-phosphate receptor (MPR), proteins

that cycle between endosomes and the trans-Golgi network (26) (Fig. 2, A and B). No colocalization of internalized SiNPs with the Golgi complex, mitochondria, or the endoplasmic reticulum was detected (data not shown), in agreement with Al-Rawi et al. (27). The accumulation of SiNPs in late endosomes/lysosomes was also observed in living cells incubated with LysoTracker Red (Fig. 2, A and B), an organic heterotricyclic 4-bora-3a,4a-diaza-s-indacene compound that accumulates within the acidic lumen of late endosomes/lysosomes. Ultrastructural analysis of HeLa cells by thin-section electron microscopy confirmed the prominent accumulation of SiNPs within the lumen of lysosomes (Fig. 2C). Lysosomal accumulation of SiNPs was paralleled by decreased metabolic activity as evidenced by the reduced ability of SiNP-treated HeLa cells to reduce the tetrazolium dye MTT (Fig. 3A). However, we did not detect pronounced cell death via apoptosis (Fig. 3B) or necrotic cell membrane permeabilization (Fig. 3C) induced by accumulation of SiNPs. Thus, dynamin 2-mediated caveolar endocytosis of SiNPs into HeLa cells resulted in their accumulation in late endosomes and lysosomes and in reduced metabolic activity of cells (consistent with Refs. 27 and 28).

The high level accumulation of SiNPs within lysosomes conceivably may perturb lysosomal function. Lysosomes are essential eukaryotic organelles that serve as endpoints for the degradation of internalized growth factors such as epidermal growth factor (EGF) (18) and for cytoplasmic material (*i.e.* aggregated proteins) targeted for autophagy, a pathway intimately linked to cellular growth control (29). Autophagy requires the posttranslational lipidation of cytoplasmic LC3 protein with phosphatidylethanolamine (a form termed LC3-II), resulting in its association with membranes and autophagosome formation. Modified LC3-II then undergoes degradation as autophagosomes fuse with lysosomes to enable degradation (29). Incubation of HeLa cells with increasing concentrations of SiNPs showed a concomitant increase in lipidated LC3-II protein (Fig. 4A) and in the number of LC3-positive autophagosomes (Fig. 4B). A similar cellular accumulation was seen for p62 (=SQSTM1) (29), another component of autophagosomes and substrate for autophagy-mediated lysosomal protein turnover (Fig. 4, A and C). As expected, LC3-positive autophagosomes displayed little overlap with LAMP1-containing lysosomes (Fig. 4E). An accumulation of LC3-containing autophagosomes was also seen in HeLa cells treated with iron-oxide NPs coated with polyethylene glycol (PEG) (Fig. 4D), suggesting that accumulation of autophagosomes may be a general phenotype induced by treatment of cells with high doses of NPs.

To further explore the mechanism underlying the observed autophagosome accumulation in SiNP-treated cells, we analyzed the effects of serum starvation, conditions that induce autophagosome formation, and of the vacuolar ATPase inhibi-

Nanoparticle-induced Lysosomal Dysfunction

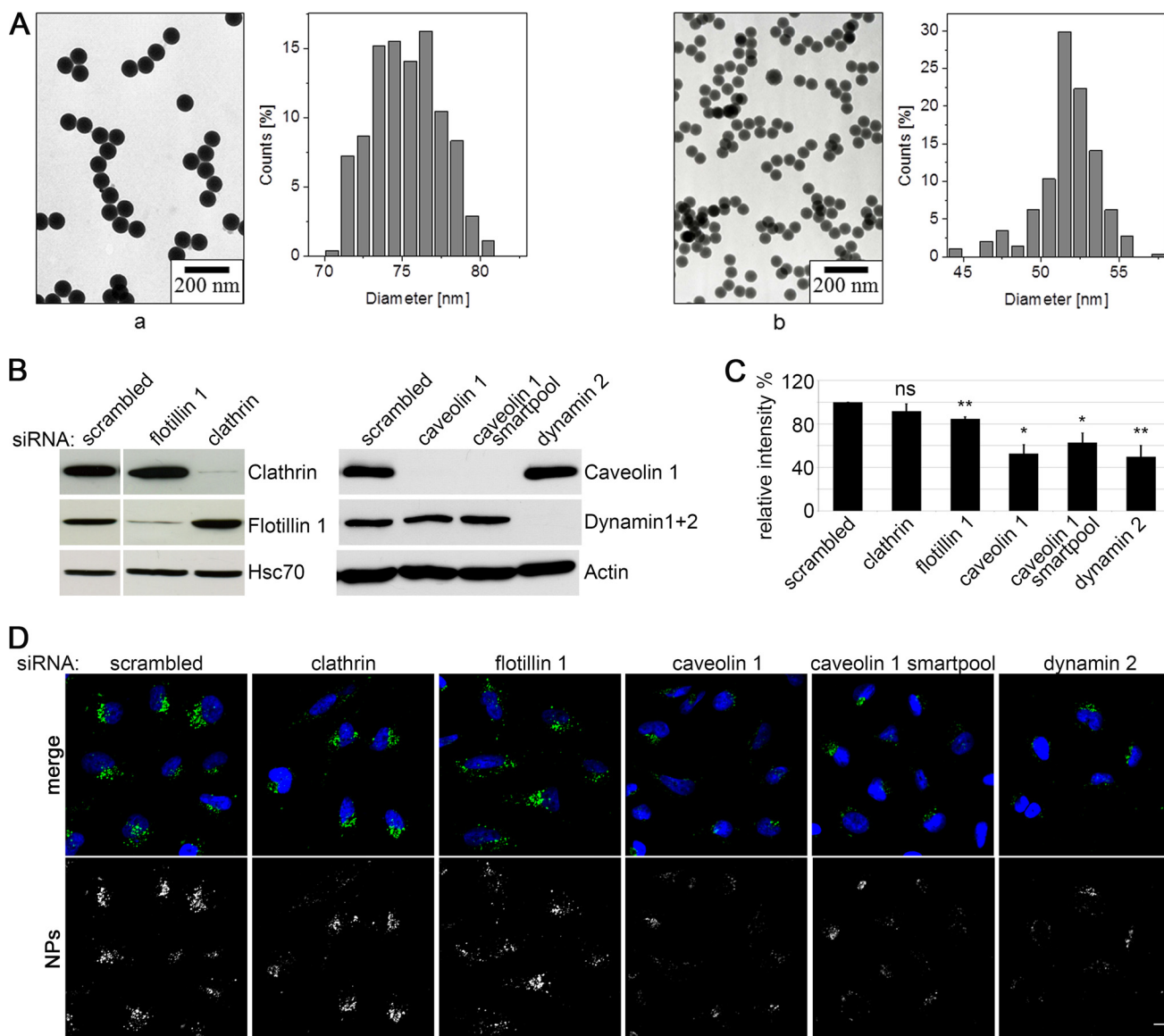


FIGURE 1. SiNPs are internalized largely via dynamin 2-mediated caveolar endocytosis. *A*, transmission electron microscopy images and corresponding size distributions of FITC-labeled SiNPs (*a*, left) and non-labeled SiNPs (*b*, right) functionalized with AHAPS. Scale bar, 200 nm. *B*, representative immunoblots of HeLa cell lysates after treatment with siRNA. Protein levels for clathrin ($4.9 \pm 2.6\%$ of control), flotillin 1 ($15.0 \pm 0.9\%$ of control), caveolin 1 ($5.1 \pm 0.9\%$ of control), or caveolin 1 smartpool ($4.4 \pm 3.6\%$ of control) and dynamin 2 (5% of control) were determined using Image J software. *C*, quantification of SiNP uptake as shown in *D*. Depicted is the mean SiNP fluorescence intensity of HeLa cells treated with siRNAs against clathrin ($91.8 \pm 6.8\%$), flotillin 1 ($84.7 \pm 2.0\%$), caveolin 1 ($52.8 \pm 8.2\%$ for single or $62.9 \pm 8.8\%$ for smartpool siRNA), or dynamin 2 ($49.9 \pm 10.3\%$) ($n = 3-10$ independent experiments; *, $p < 0.05$; **, $p < 0.01$). *ns*, not significant. *D*, Representative confocal microscopy images of HeLa cells incubated with SiNPs after depletion of clathrin, flotillin 1, caveolin 1 (single or smartpool siRNA), or dynamin 2. Scale bar, 10 μm .

TABLE 1

Characterization of SiNPs with (+) and without (–) FITC in the core

Data are from $n = 5$ independent measurements (at 25 °C, in DMEM (+10% FCS) at 37 °C) performed within the first hour after transfer into the corresponding medium. TRM, transmission electron microscopy; DLS, differential light scattering. \varnothing = diameter; ζ = zeta potential.

Nanoparticle type	Ethanol			Water		DMEM (+ 10% FCS)
	\varnothing /nm (TEM)	\varnothing /nm (DLS)	ζ /mV	\varnothing /nm (DLS)	ζ /mV	\varnothing /nm (DLS)
SiNPs (+FITC)	75 ± 2	107 ± 1	$+51 \pm 1$	119 ± 2	$+25 \pm 1$	245 ± 4
SiNPs (–FITC)	52 ± 2	105 ± 3	$+37 \pm 7$	118 ± 6	$+33 \pm 2$	150 ± 15

tor bafilomycin A1, which blocks lysosomal degradation by dissipating the lysosomal proton gradient. Starvation of control cells resulted in increased levels of lipidated LC3-II due to the

accumulation of LC3-positive autophagosomes, and this phenotype was exacerbated by concomitant application of bafilomycin A1 to prevent lysosomal turnover of autophagosomes (Fig. 5, A and C). Cells treated with SiNPs displayed high levels of lipidated LC3-II and accumulated LC3-positive autophagosomes under all conditions, largely irrespective of whether cells had been starved and/or treated with bafilomycin A1 (Fig. 5, A and C). Treatment of cells with non-fluorescent, unlabeled SiNPs also caused LC3-II to accumulate (Fig. 5B). These data suggest that lysosomal accumulation of SiNPs within cells is not due to enhanced autophagosome formation but may rather reflect defective autophagic flux.

Consistent with these results, we found that accumulation of autophagosomes and of p62 were not a consequence of altered

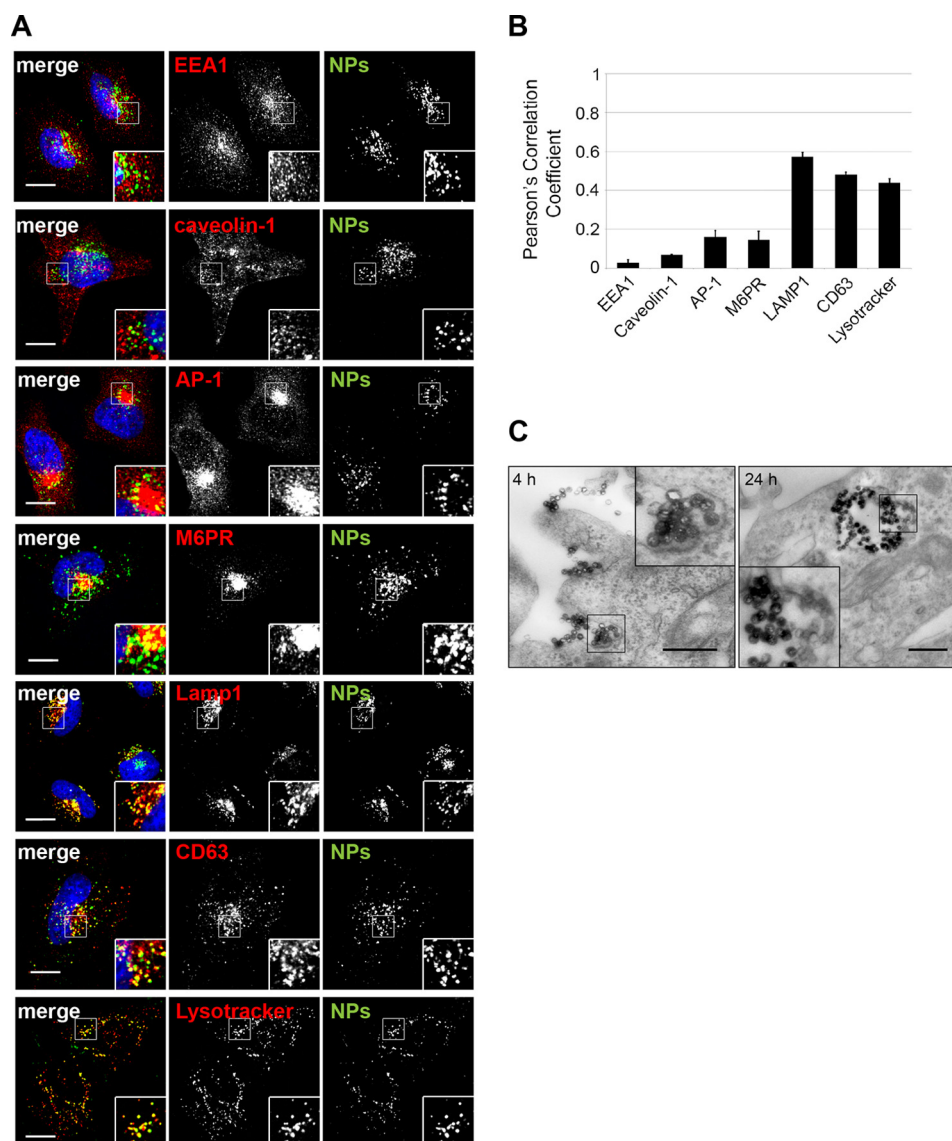


FIGURE 2. SiNPs accumulated in lysosomes. *A*, confocal microscopy images of HeLa cells illustrating the subcellular localization of internalized SiNPs after 4 h (green channel) and various organellar markers (red channel). EEA1 and the caveolar marker protein caveolin-1 do not colocalize with internalized SiNPs. There is a partial colocalization of SiNPs with the trans-Golgi network/endosomal proteins AP-1 and mannose 6-phosphate receptor (M6PR). SiNPs strongly colocalize with the lysosomal membrane protein LAMP1 and CD63. A profound colocalization of SiNPs with lysosomes was also observed in living cells after incubation with LysoTracker Red. Scale bar, 10 μ m. *B*, Pearson's correlation coefficients of SiNPs with different organellar markers: EEA1 (early endosomes), 0.080 ± 0.014 ; caveolin 1 (caveolae), 0.068 ± 0.001 ; AP-1 (trans-Golgi network/recycling endosomes), 0.161 ± 0.032 ; M6PR (trans-Golgi network/endosomes), 0.212 ± 0.008 ; LAMP1 (late endosomes/lysosomes), 0.396 ± 0.023 ; CD63 (late endosomes/lysosomes), 0.474 ± 0.012 ; LysoTracker (lysosomes), 0.439 ± 0.021 . $n = 3$ independent experiments. *C*, electron micrographs of lysosomes acquired after 4 h (left) or 24 h (right) of HeLa cell incubation with SiNPs. Scale bars, 500 nm.

mTOR signaling, a key regulatory pathway of autophagy, as the cellular accumulation of SiNPs did not alter the levels of phospho-S6K1 or phospho-ULK1 (Fig. 6). We conclude that intralysosomal accumulation of SiNPs leads to the accumulation of p62-containing LC3-positive autophagosomes that apparently fail to undergo further lysosomal degradation as further explored in detail below (see Fig. 9).

Although these results indicate that cellular accumulation of SiNPs impairs degradation of cytoplasmic proteins targeted for lysosomal degradation via autophagy, they do not address whether growth factors internalized from the plasma membrane via endosomes can be degraded efficiently in SiNP-filled lysosomes. We, therefore, analyzed the uptake and degradation of Alexa647-labeled EGF. Endocytosis of EGF-Alexa647 into

HeLa cells proceeded unaltered irrespective of whether or not these cells had been incubated with SiNPs before EGF addition (Fig. 7C, 30 min). SiNP-treated cells also showed normal surface levels of EGF receptors, and ligand binding to these receptors elicited a signaling response similar to that of control cells (Fig. 7, D and E). However, SiNP-containing HeLa cells displayed a strongly reduced ability to degrade internalized EGF-Alexa647 during the subsequent post-endocytic chase period of 60 or 120 min (Fig. 7C). Instead of being rapidly degraded, a significant fraction of internalized EGF-Alexa647 remained within punctuate structures identified by multicolor confocal microscopy as LAMP1- and CD63-positive late endosomes even after a 120-min chase (Fig. 7, F and G). This effect was specific for the lysosomal system as endocytosis and recycling

Nanoparticle-induced Lysosomal Dysfunction

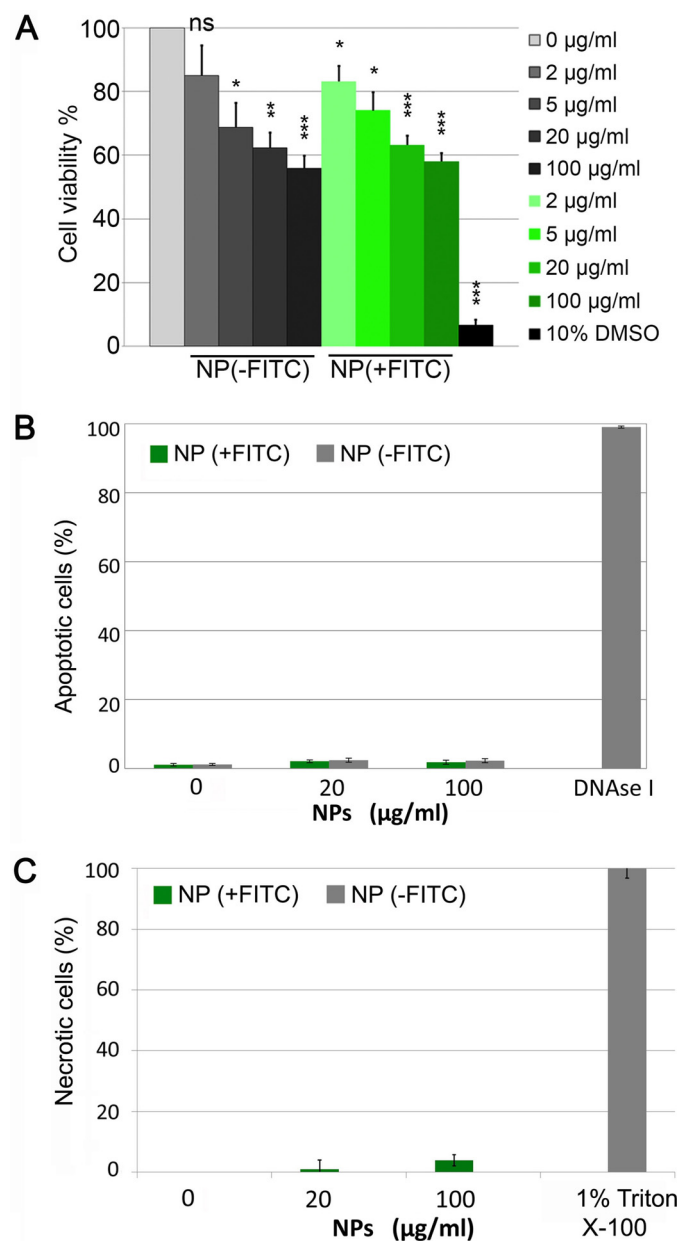


FIGURE 3. SiNPs accumulation in lysosomes reduced metabolic activity but did not induce apoptotic or necrotic death of cells. *A*, reduced metabolic activity of SiNP-treated (24 h) HeLa cells assayed by MTT. Viability was determined for cells treated with 2 $\mu\text{g ml}^{-1}$ SiNPs ($85.0 \pm 9.4\%$ (-FITC) and $83.1 \pm 4.9\%$ (+FITC)) with 5 $\mu\text{g ml}^{-1}$ SiNPs ($68.8 \pm 7.6\%$ (-FITC) and $74.0 \pm 5.8\%$ (+FITC)), with 20 $\mu\text{g ml}^{-1}$ SiNPs ($62.3 \pm 4.8\%$ (-FITC) and $63.2 \pm 2.9\%$ (+FITC)), and 100 $\mu\text{g ml}^{-1}$ SiNPs ($55.8 \pm 4.0\%$ (-FITC) and $58.0 \pm 2.6\%$ (+FITC), respectively). *ns*, non-significant; *, $p < 0.05$; **, $p < 0.01$; ***, $p < 0.001$. *B*, SiNP treatment of HeLa cells does not induce apoptotic cell death. Apoptotic cell death of HeLa cells treated for 24 h with 20 $\mu\text{g ml}^{-1}$ or 100 $\mu\text{g ml}^{-1}$ SiNPs analyzed by TUNEL staining. Cells treated with DNase I for 15 min served as a positive control. *C*, SiNP treatment of HeLa cells does not induce necrotic cell death. Necrotic cell death of HeLa cells treated for 24 h with 20 $\mu\text{g ml}^{-1}$ or 100 $\mu\text{g ml}^{-1}$ SiNPs analyzed by lactate dehydrogenase (LDH) release into the medium. Lactate dehydrogenase activity released by complete lysis of HeLa cells after treatment with 1% Triton X-100 was set to 100%.

of transferrin, an iron-carrying protein not degraded via lysosomes, from endosomes to the cell surface proceeded unperturbed (Fig. 7, *A* and *B*). Intralysosomal accumulation of SiNPs in HeLa cells, thus, disrupts the lysosomal degradation of internalized EGF and likely of other growth and differentiation factors.

What might be the reason for the failure of SiNP-filled lysosomes to degrade cytoplasmic autophagic substrates or internalized growth factors? Several scenarios can be envisioned. Lysosomes containing AHAPS-modified SiNPs may be dysfunctional because their proton gradient is disrupted due to the accumulation of charge, sequestration of ions required for acidification (*i.e.* Cl^-), or loss of membrane integrity. Such changes would eventually result in the inactivity of intralysosomal hydrolases (17). Alternatively, SiNP-filled lysosomes may be unable to receive cargo from upstream donor compartments such as autophagosomes and late endosomes, *i.e.* due to the inability of their limiting membrane to undergo remodeling required for fusion, resulting in the spatial segregation of lysosomes from their target substrates (19). We tested these possibilities by first analyzing lysosomal pH in living cells. Ratiometric imaging using pH-sensitive Oregon Green488 coupled to 10-kDa dextran (30) revealed an intralysosomal pH of 4.5 ± 0.1 in control cells and of 3.9 ± 0.1 in SiNP-loaded cells (Fig. 8, *A–C*). The slightly lower pH of SiNP-loaded lysosomes possibly is a secondary consequence resulting from the failure of these lysosomes to degrade intracellular proteins, which serve as the main luminal buffer for protons. Consistent with this and with the fact that most lysosomal hydrolases are activated by low pH, we observed elevated cathepsin B and L activities in SiNP-loaded cells (Fig. 8, *D–F*). These data show that dysfunction of SiNP-filled lysosomes is not the result of impaired lysosomal acidification or inactivity of intralysosomal hydrolases.

We, therefore, finally tested the hypothesis that impaired autophagy and lysosomal degradation result from impaired cargo delivery to lysosomes from upstream donor compartments such as autophagosomes and late endosomes. If this indeed were the case, one would expect that substrates for lysosomal proteolysis such as LC3-II, p62, and internalized EGF accumulate in compartments lacking SiNPs as well as functional lysosomal hydrolases. Multicolor confocal imaging indeed revealed the near complete lack of colocalization between LC3-, p62-, and SiNP-containing lysosomes (*e.g.* positive for cathepsin B/L), whereas SiNPs displayed a profound overlap with lysosomal cathepsin B and L hydrolase activities (Fig. 9, *A* and *B*). To directly test the hypothesis that impaired autophagy and lysosomal degradation result from impaired cargo delivery to lysosomes from upstream compartments, we used tandem RFP-GFP-tagged LC3. Fusion of RFP-GFP-LC3 with lysosomes results in quenching of GFP fluorescence and, thus, has been widely used to monitor autophagic flux and autolysosome formation. Serum starvation induced autolysosome formation in control cells, and this was completely blocked by treatment of cells with the vacuolar ATPase inhibitor bafilomycin A1 as expected (Fig. 9*C*, *no NPs*). By contrast, autolysosome formation was significantly impaired in SiNP-treated cells irrespective of whether cells were fed or serum-starved (Fig. 9*C*, +100 $\mu\text{g/ml}$ NPs).

Collectively, these data demonstrate that impaired autophagic protein turnover and degradation of internalized growth factors in SiNP-treated cells likely results from inhibition of cargo delivery via autophagosomes and late endosomes to SiNP-filled lysosomes.

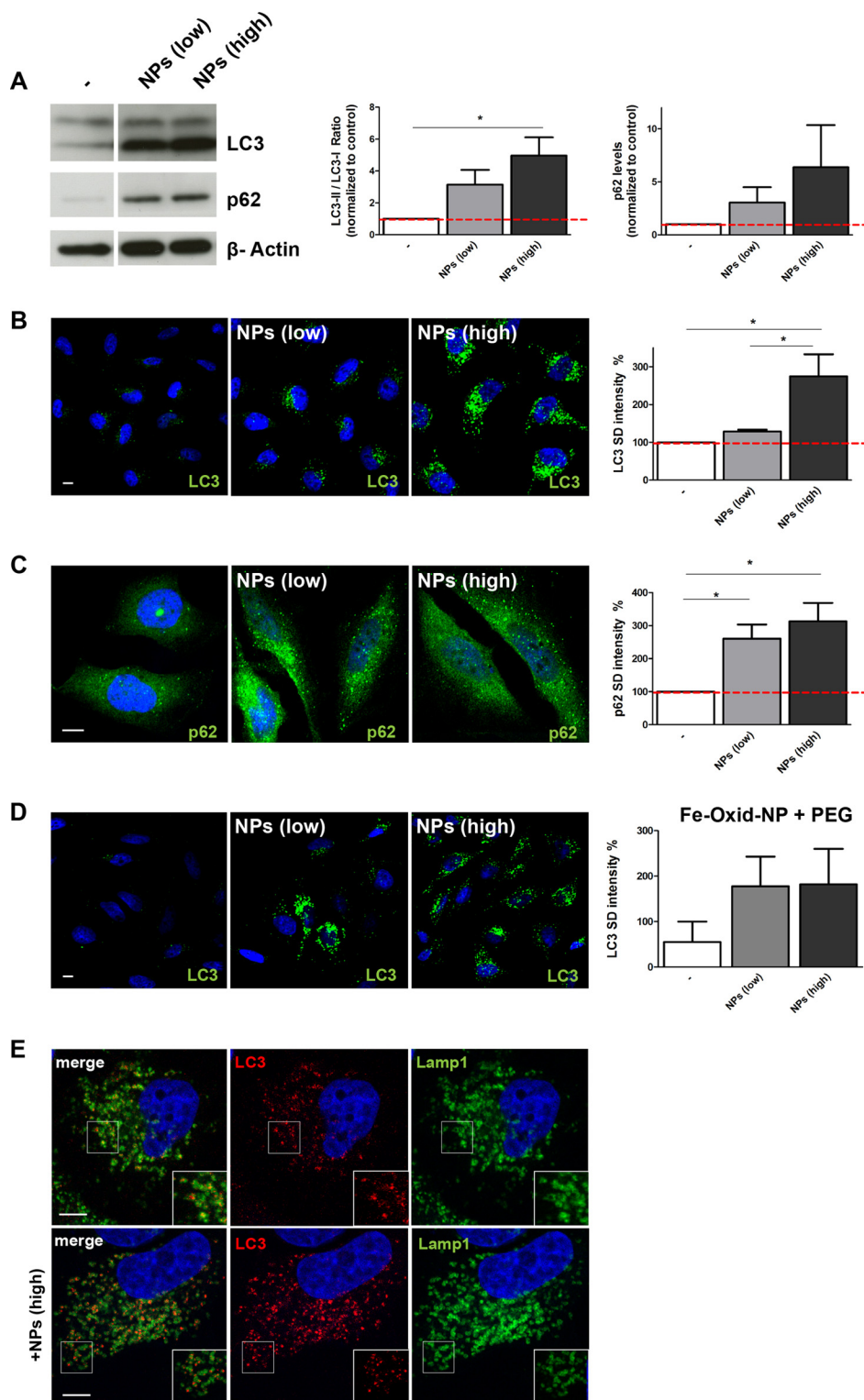


FIGURE 4. Effects on autophagy in SiNP-loaded cells. *A*, immunoblot analysis of control cells or cells treated with 20 $\mu\text{g/ml}$ SiNPs (*NPs (low)*) or 100 $\mu\text{g/ml}$ SiNPs (*NPs (high)*) for LC3-I (inactive precursor), LC3-II (the active autophagosome-associated form), and p62. The LC3-II/LC3-I ratio was quantified and normalized to control cells: control (set to 1); *NPs (low)* (3.1 ± 0.9); *NPs (high)* (5.0 ± 1.2). p62 quantification: control (set to 1); *NPs (low)* (3.04 ± 1.4); *NPs (high)* (6.38 ± 3.9). $n = 4$ independent experiments; *, $p < 0.05$. *B*, *left*, confocal images of control or SiNP-treated HeLa cells (*low*, 20 $\mu\text{g/ml}$; *high*, 100 $\mu\text{g/ml}$) stained for the autophagosomal marker LC3. *Right*, quantification of LC3 intensity levels in control cells (set to 100%) and in cells incubated with low NPs ($129.1 \pm 4.6\%$) and high NPs ($274.8 \pm 58.6\%$). Values represent the mean \pm S.E. for $n = 4$ independent experiments; *, $p < 0.05$. *C*, *left*, confocal images of control or SiNP-treated HeLa cells (*low*, 20 $\mu\text{g/ml}$; *high*, 100 $\mu\text{g/ml}$) stained for the autophagic marker p62. *Right*, quantification of p62 intensity levels in control cells (set to 100%) and in cells incubated with low NPs ($260.9 \pm 42.4\%$) and with high NPs ($313.3 \pm 55.4\%$). Data represent mean \pm S.E., $n = 3$ independent experiments; *, $p < 0.05$. *D*, *left*, confocal images of control or Fe₂O₃-NP-treated HeLa cells (*low*, 20 $\mu\text{g/ml}$; *high*, 100 $\mu\text{g/ml}$) stained for the autophagosomal marker LC3. *Right*, quantification of LC3 intensity levels in control cells (set to 100%) and in cells incubated with low NPs ($177.87 \pm 65.3\%$) and with high NPs ($182.64 \pm 78.3\%$). Data represent mean \pm S.E., $n = 2$ independent experiments. *E*, representative confocal images of HeLa cells treated or not with 100 $\mu\text{g/ml}$ SiNPs (*NPs (high)*) and co-stained for LC-3 and LAMP1. Scale bar, 10 μm .

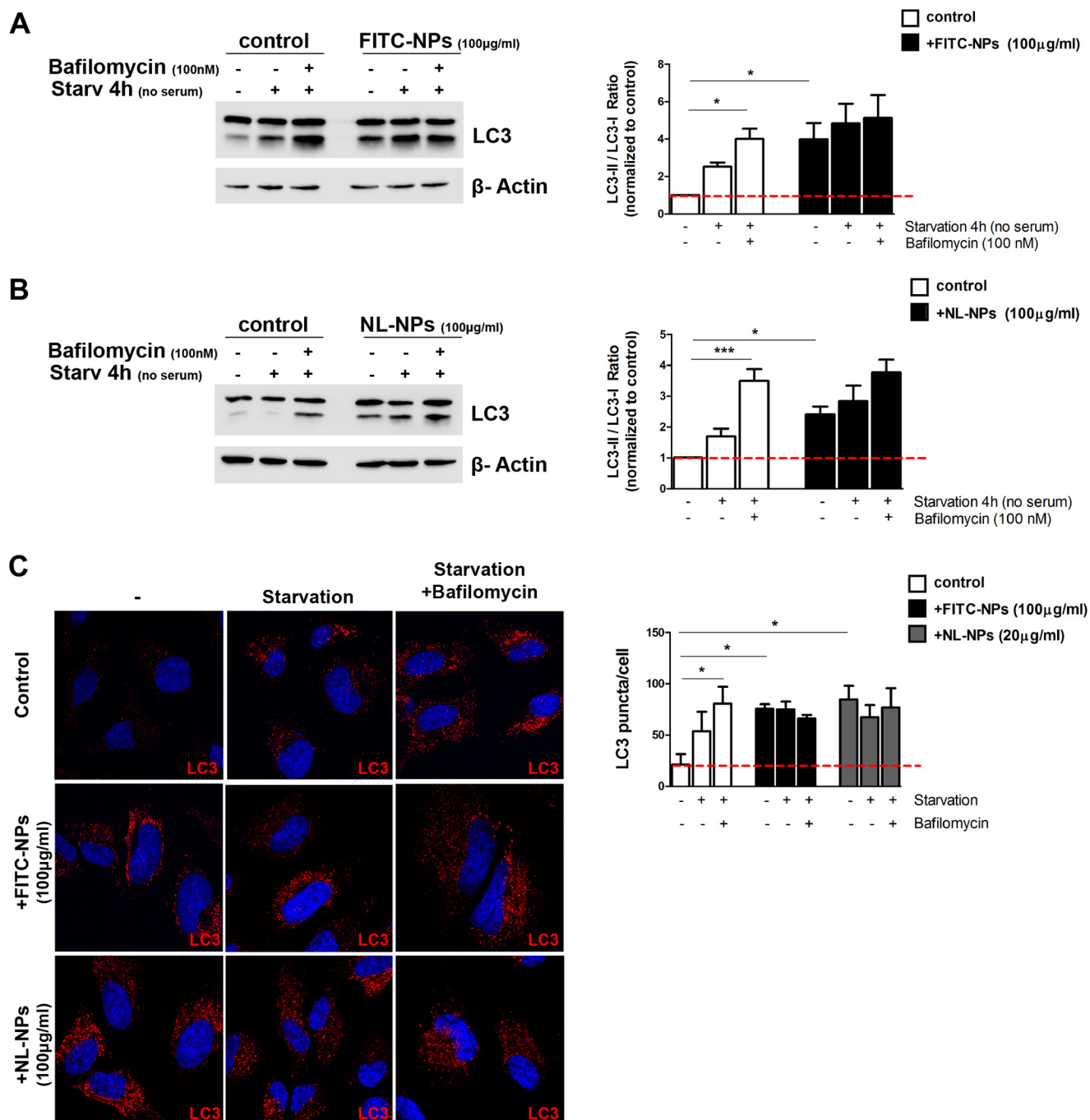


FIGURE 5. SiNPs induced the accumulation of autophagy markers by blocking autophagic flux. *A*, untreated or treated HeLa cells with 100 µg/ml FITC-labeled SiNPs (FITC-NPs) for 24 h were incubated in complete DMEM medium and in serum-free starvation medium for 4 h in the presence or absence of bafilomycin A1 and then analyzed by Western blotting for the autophagosomal marker LC3. The LC3-II/LC3-I ratio was quantified and normalized to untreated control cells. Shown are non-starved control cells (set to 1), starved control cells (2.52 ± 0.2), starved control cells treated with 100 nM bafilomycin A1 (4.002 ± 0.5), non-starved cells incubated with FITC-NPs (3.98 ± 0.87), starved FITC-NPs-treated cells in the absence (4.84 ± 1) or presence of 100 nM bafilomycin A1 (5.13 ± 1.2). Data are the mean \pm S.E.; $n = 4$ independent experiments; *, $p < 0.05$. *B*, untreated or treated HeLa cells with 100 µg/ml non-labeled SiNPs (NL-NPs) were incubated as above and then analyzed by Western blotting LC3. The LC3-II/LC3-I ratio was quantified and normalized to untreated control cells. Shown are non-starved control cells (set to 1), starved control cells (1.69 ± 0.2), starved control cells treated with 100 nM bafilomycin A1 (3.49 ± 0.3), non-starved cells incubated with NL-NPs (2.41 ± 0.2), starved NL-NP-treated cells in the absence (2.83 ± 0.5) or presence of 100 nM bafilomycin A1 (3.76 ± 0.4). Data are the mean \pm S.E.; $n = 4$ independent experiments; *, $p < 0.05$; ***, $p < 0.001$. *C*, *left*, confocal images of untreated or treated HeLa cells with 100 µg/ml FITC-NPs or NL-NPs and incubated as above. After fixation, cells were stained for LC3. *Right*, quantification of LC3 puncta per cell of every condition: non-starved control cells (21.37 ± 10), starved control cells (53.63 ± 19), starved control cells treated with 100 nM bafilomycin A1 (80.61 ± 16.6), non-starved cells incubated with FITC-NPs (75.56 ± 4.5), starved FITC-NP-treated cells in the absence (74.99 ± 7.5) or presence of 100 nM bafilomycin A1 (66.11 ± 3.5), non-starved cells incubated with NL-NPs (84.72 ± 13.3), starved NL-NP-treated cells in the absence (67.47 ± 11.7) or presence of 100 nM bafilomycin A1 (76.96 ± 18.7). Data are the mean \pm S.E.; $n = 3$ independent experiments; *, $p < 0.05$.

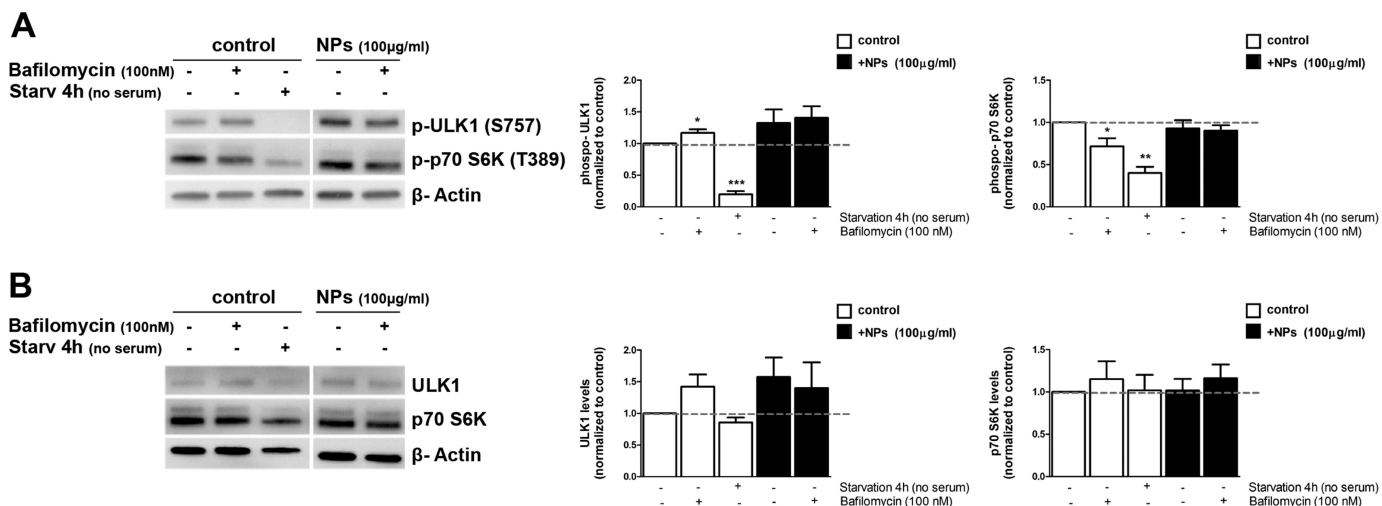


FIGURE 6. **Lysosomal SiNP accumulation did not alter mTORC1 signaling.** *A, left*, immunoblot analysis of control cells or cells treated with 100 μ g/ml SiNPs for phospho-ULK1 (Ser-757) and phospho-p70 S6K (Thr-389). Baf A1 (100 nM) was added to the medium (for 4 h) where indicated. Actin served as loading control. *Middle*, quantification of phospho-ULK1: non-starved (set to 1), non-starved + Baf A1 (1.12 \pm 0.06), starved (0.22 \pm 0.08), SiNPs (1.12 \pm 0.08), SiNPs + Baf A1 (1.26 \pm 0.19). *Right*, quantification of phospho-S6K: non-starved (set to 1), non-starved + Baf A1 (0.72 \pm 0.10), starved (0.40 \pm 0.07), SiNPs (0.93 \pm 0.10), SiNPs + Baf A1 (0.90 \pm 0.07). *B, left*, immunoblot analysis of control cells or cells treated with 100 μ g/ml SiNPs for total levels of ULK1 and p70 S6K. Baf A1 (100 nM) was added to the medium (for 4 h) where indicated. Actin served as the loading control. *Middle*, quantification of total-ULK1: non-starved (set to 1), non-starved + Baf A1 (1.4 \pm 0.2), starved (0.9 \pm 0.1), NPs (1.6 \pm 0.3), NPs + Baf A1 (1.4 \pm 0.4). *Right*, quantification of total p70 S6K: non-starved (set to 1), non-starved + Baf A1 (1.2 \pm 0.2), starved (1.0 \pm 0.2), NPs (1.0 \pm 0.1), NPs + Baf A1 (1.2 \pm 0.2). Data are presented as the mean \pm S.E. for $n = 3$ independent experiments; *, $p < 0.05$; **, $p < 0.01$; ***, $p < 0.001$.

Discussion

We demonstrate using siRNA-mediated cellular depletion of key endocytic proteins that positively charged SiNPs enter cells largely (though perhaps not exclusively) via dynamin 2-dependent caveolar internalization rather than clathrin-mediated endocytosis in contrast to a previous study (12). We also observed a small inhibitory effect of flotillin 1 depletion on SiNP uptake that may reflect a secondary caveolin-independent endocytic pathway or, alternatively, the use of shared components of caveolar- and CLIC/GEEC-mediated endocytosis described recently (31).

The most important conclusion that emanates from our work is the fact that positively charged SiNPs and by extension other SiNPs that accumulate in lysosomes (28), although generally perceived as being well tolerated by mammalian cells, accumulate in lysosomes over extended periods of times (we have followed them for days without loss of signal) causing impairment of lysosomal function, a pathway not addressed in prior studies (for example, see Refs. 27 and 28). Several lines of evidence support this. First, we show that lysosomal accumulation of SiNPs causes the accumulation of LC3- and p62-positive autophagosomes that fail to undergo lysosomal degradation, suggesting that degradation of cytosolic proteins via autophagy is perturbed. Second, we demonstrate that SiNP-treated cells partially fail to degrade exogenous ligands such as growth factors (*i.e.* EGF), which instead accumulate in late endosomes. By contrast, endosomal recycling proceeds unperturbed, indicating that SiNP-induced alterations within the endosomal system are specific for degradative sorting. Degradation of internalized growth and differentiation factors is an important means of mammalian cells to control cell growth and entry into mitosis (18). Third, we show that failed lysosomal proteolysis of EGF or autophagosomal substrates does not result from altered mTOR signaling, elevated intralysosomal pH, or general damage of lyso-

somal membranes. Furthermore, qualitative cathepsin activity assays argue against SiNP-induced impairment of lysosomal protease activity, although quantitative effects of SiNPs on cathepsin trafficking or activation cannot be ruled out completely.

Rather, we favor a model according to which lysosomes containing high levels of SiNPs fail to receive cargo from late endosomes and autophagosomes, *i.e.* due to defective fusion of these organelles with lysosomes (Fig. 10) as evidenced by the observed spatial segregation of non-degraded EGF or p62 and lysosomal proteases (Fig. 9, *A* and *B*) and the impaired autophagic flux and autolysosome formation (Fig. 9C) in SiNP-treated cells. At the moment we can only speculate why SiNP-containing lysosomes maybe fusion-defective. One possibility is that the rigid structure of SiNPs, perhaps paired with electrostatic interactions of their positively charged surface with negatively charged glycolipids lining the luminal face of lysosomal membranes (32), may prevent membrane remodeling processes that are required for SNARE-mediated fusion with late endosomes or autophagosomes (33). Consistent with this possibility, it has been observed that membrane fission at the plasma membrane is regulated by the specific lipid environment (34). However, other mechanisms of SiNP action on lysosomal fusion cannot be ruled out.

Given that lysosomal function is key to many aspects of cell physiology, most notably the clearance of degradation-prone (*i.e.* internalized growth factors), aggregated malfunctioning proteins (17, 29, 35), we hypothesize that the adverse effects of SiNPs on the metabolic activity of cells are a direct consequence of lysosomal dysfunction. Accumulation of NPs in cells, in particular in the brain, apart from the effects on cell metabolism may potentially also affect the clearance of aggregated proteins via autophagy and, thus, favor neurodegenerative disorders such as Morbus Alzheimer, Huntington disease, or Parkinson disease (35). Irrespective of whether some or all of these effects are of clinical rele-

Nanoparticle-induced Lysosomal Dysfunction

vance, our data call for a reassessment of the risk associated with the application of SiNPs in biomedicine.

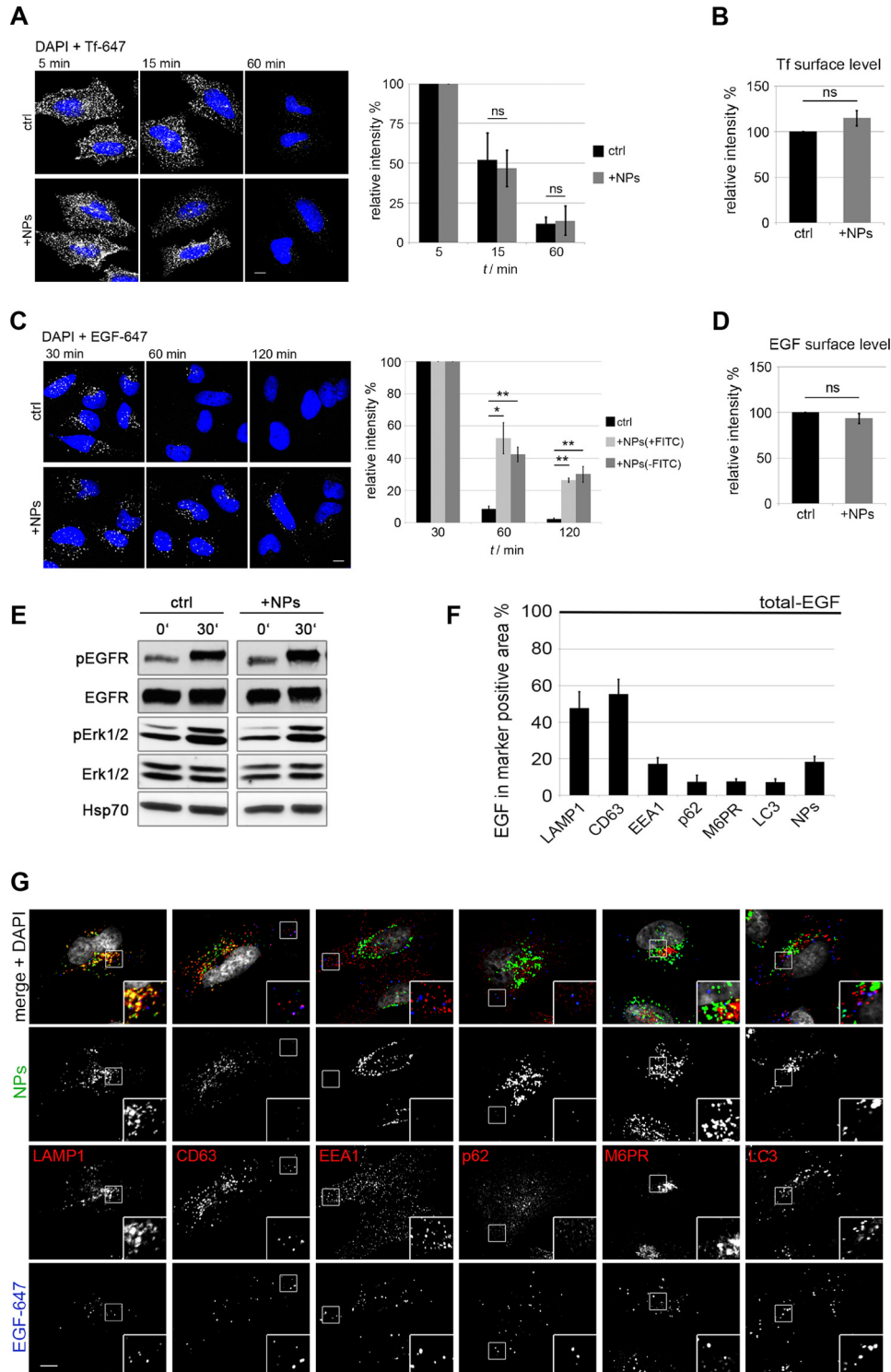
Experimental Procedures

NP Synthesis and Characterization (Transmission Electron Microscopy, Dynamic Scattering, Zeta Potential)

The synthesis and characterization of SiNPs were performed as previously described (22). Super-paramagnetic Fe₂O₃-NPs were a kind gift of MagForce AG (Berlin).

Cell Culture and Transfection

HeLa cells were grown in low glucose Dulbecco's modified Eagle's medium (DMEM) supplemented with 10% (v/v) fetal bovine serum (FBS), 1% glutamine, and 1% penicillin/streptomycin and cultured at 37 °C, 5% CO₂. SiRNA transfections were done with Oligofectamine (Invitrogen). HeLa cells were transfected with the mRFP-GFP-LC3 plasmid using lipofectamine2000 (Invitrogen). After transfection, cells were



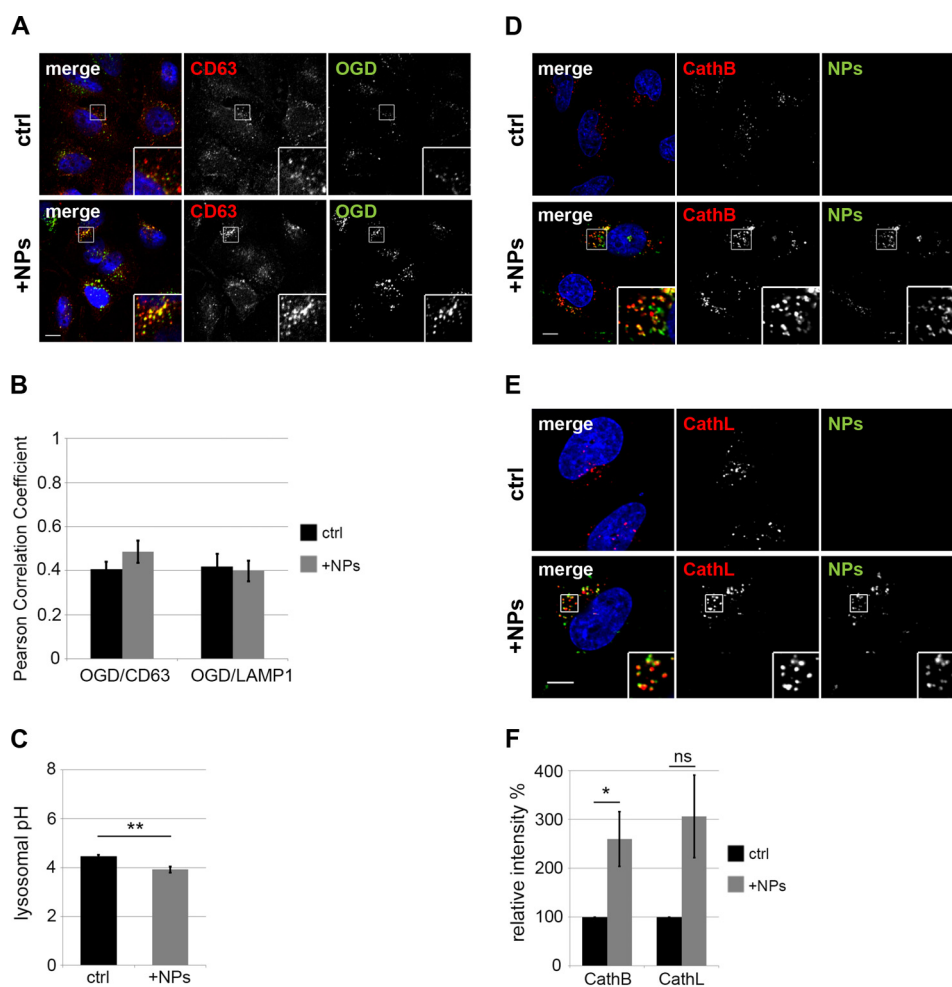


FIGURE 8. Effects of SiNP accumulation in lysosomes on lysosomal acidification and cathepsin activity. *A*, representative confocal images showing colocalization of OGD with the late endosomal/lysosomal marker CD63 in control (*ctrl*) and SiNP-treated HeLa cells shown by confocal imaging. *B*, quantitative analysis of data shown in *A*. Pearson's correlation coefficients were determined for OGD and CD63 (*ctrl*, 0.41 ± 0.03; +NPs, 0.49 ± 0.05, respectively) and OGD and LAMP1 (*control*, 0.42 ± 0.06; +NPs, 0.40 ± 0.05, respectively), mean ± S.E.; *n* = 3 independent experiments. *C*, SiNP accumulation does not impair lysosomal acidification. Ratiometric measurement of intralysosomal pH of control (*ctrl*, pH 3.9 ± 0.1) or SiNP-treated HeLa cells (+NPs, pH 4.5 ± 0.1) Data are the mean ± S.E.; *n* = 5 independent experiments; **, *p* < 0.01. *D* and *E*, live cell confocal images show the localization of hydrolyzed fluorescent cathepsin B (*D*) or cathepsin L (*E*) products (red) in the control (*upper panel*) and SiNP (*green*)-treated HeLa cells (*lower panel*). Elevated activities of cathepsins B (259.8 ± 56.1%) and L (306.5 ± 84.5%) in SiNP-treated HeLa cells compared with controls (set to 100%). Data are the mean ± S.E., *n* = 3 independent experiments; *, *p* < 0.05. *ns*, not significant.

FIGURE 7. SiNP accumulation did not affect endocytosis or recycling of Tf but impaired EGF degradation and resulted in the accumulation of non-degraded EGF in late endosomes. *A*, confocal microscopy images show Alexa647-transferrin (Tf-647) levels in control (*ctrl*) and SiNP-treated (+NPs) HeLa cells at three different time points. Nuclei were stained with DAPI (blue). Quantified is the Tf-647 fluorescence intensity in cells incubated with SiNPs (+NPs) compared with control cells (*ctrl*). Intensity values at 5 min were set to 100% to monitor the recycling process. At 15 min post-chase with unlabeled Tf the levels of Tf-647 were reduced to 52 ± 17% in control cells versus 47 ± 11% in SiNP-treated cells. At 60 min post-chase with unlabeled Tf levels of Tf-647 were reduced to 12 ± 4% in control (control) cells versus 14 ± 9% in SiNP-treated cells. Data represent the mean ± S.E., *n* = 3 independent experiments. Scale bar, 10 μm. *ns*, not significant. *B*, unaltered surface levels of Tf receptors in control (*ctrl*) (set to 100%) and SiNP-treated HeLa cells (+NPs) (115 ± 8%, *ns* = non-significant). HeLa cells were incubated with Tf-647 at 4 °C to allow for Tf receptor engagement in the absence of internalization, washed extensively, and analyzed by immunofluorescence microscopy. Data represent the mean ± S.E., *n* = 4 independent experiments. *C*, left, confocal images of Alexa647-EGF (red) internalized into control (*ctrl*) or SiNP (green)-treated HeLa cells chased for the indicated time points post-internalization. DAPI (blue), nuclei. Right, quantitation of Alexa647-EGF fluorescence intensity of control (*ctrl*) or SiNP-treated HeLa cells (+NPs, either FITC-labeled (+FITC) or unlabeled (-FITC)). Intensity values at 30 min were set to 100%. Degradation of EGF was significantly impaired at 60 min (EGF remaining: control (8.4 ± 1.9%) versus NP+FITC (52.4 ± 9.6%); NP-FITC, 42.3 ± 4.5%) and 120 min of chase (EGF remaining: control (2.2 ± 0.7%) versus NP+FITC (26.3 ± 1.3%) and NP-FITC, 30.1 ± 4.8%) in SiNP-treated cells. Data are the mean ± S.E., *n* = 3 independent experiments; *, *p* < 0.05; **, *p* < 0.01; ***, *p* < 0.001. Scale bar, 10 μm. *D*, unaltered surface levels of EGF receptors in control (*ctrl*) (set to 100%) and SiNP-treated HeLa cells (+NPs) (93.3 ± 5.3%) kept at 4 °C. Data are the mean ± S.E., *n* = 4 independent experiments. *E*, immunoblot analysis of EGF signaling responses of control (*ctrl*) or SiNP-treated HeLa cells. Shown are immunoblots for: phosphorylated EGF receptor (pEGFR), total EGF receptor (EGFR), phosphorylated Erk1/2 kinase (pErk 1/2), and total Erk1/2 kinase (Erk). Hsp70 served as the loading control. *F*, non-degraded EGF accumulates in late endosomes. Confocal microscopy analysis of the localization of non-degraded Alexa647-EGF accumulated in SiNP-treated HeLa cells. Fraction of Alexa647-EGF in immunopositive compartments: LAMP1 (late endosomes/lysosomes), 47.79 ± 0.09%; CD63 (late endosomes/lysosomes), 55.38 ± 0.08%; EEA1 (early endosomes), 17.22 ± 0.03%; p62 (autophagosomes), 7.43 ± 3.42%; M6PR (trans-Golgi network/endosomes), 7.48 ± 1.49%; LC3 (autophagosomes), 7.16 ± 1.83%. Data are the mean ± S.E., *n* = 3 independent experiments. *G*, non-degraded EGF accumulates in late endosomes. Representative confocal images of SiNPs-treated HeLa cells 120 min after the addition of Alexa647-EGF. To assess the localization of non-degraded EGF, cells were counterstained for different organellar markers: LAMP1 (late endosomes/lysosomes), CD63 (late endosomes/lysosomes), EEA1 (early endosomes), p62 (autophagosomes), M6PR (trans-Golgi network/endosomes), or LC3 (autophagosomes). Scale bar, 10 μm.

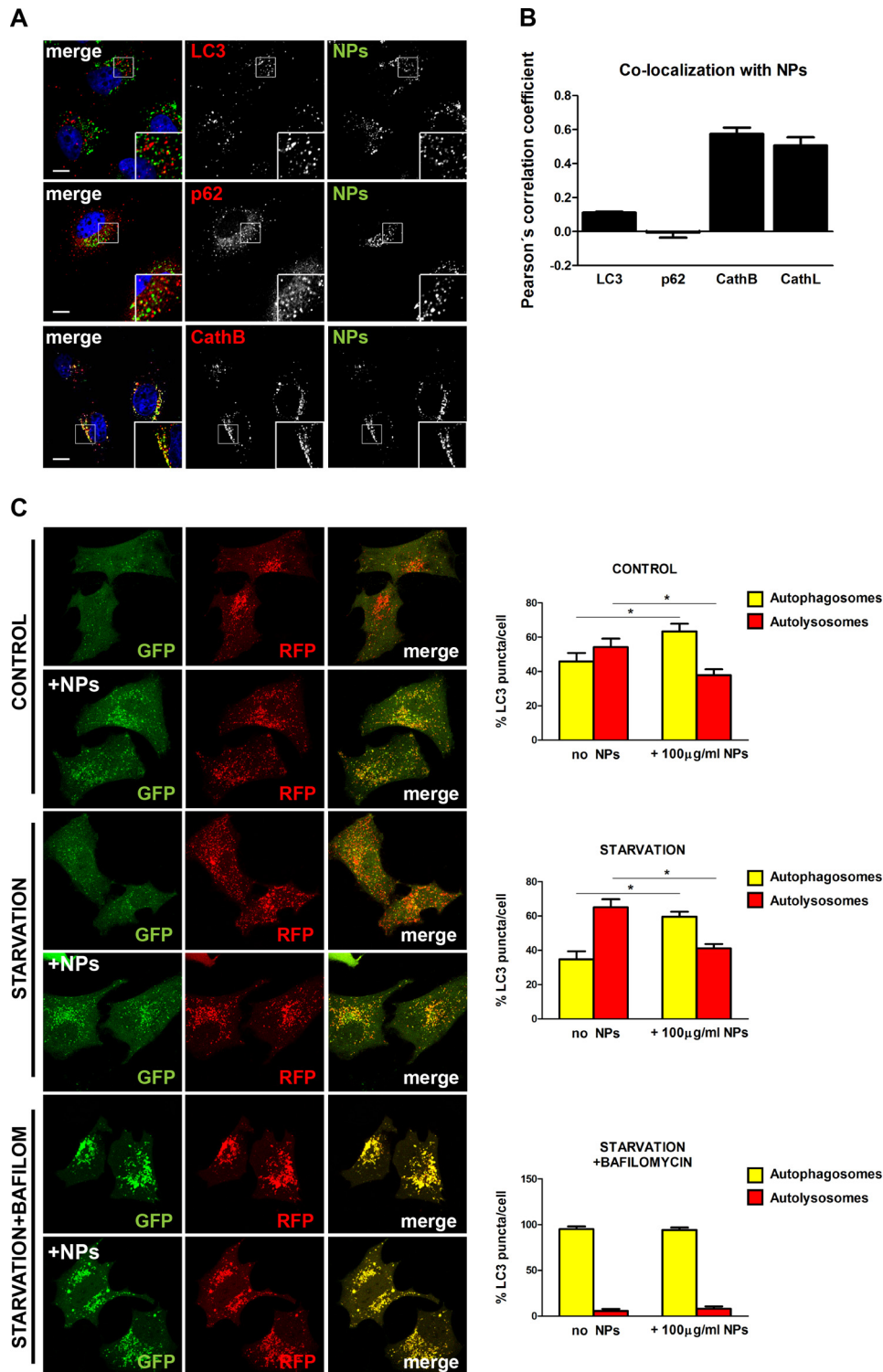


FIGURE 9. **Lysosomal accumulation of SiNPs impaired autophagosome-lysosome fusion.** *A*, representative confocal images depicting the distribution of LC3, p62 and cathepsin B (red channel)- in FITC-SiNP (green)-treated HeLa cells. Scale bars, 10 μm. *B*, quantitative analysis of data shown in *A*. Pearson's correlation analysis shows lack of colocalization between LC3 (0.111 ± 0.006) and p62 (-0.005 ± 0.031) with SiNPs. Fluorescent cathepsin products strongly colocalize with SiNPs (0.58 ± 0.04 for cathepsin B and 0.51 ± 0.05 for cathepsin L). Data are the mean ± S.E., *n* = 3 independent experiments. *C*, HeLa cells were transiently transfected with an RFP-GFP tandem fluorescently-tagged LC3. After 24 h, cells were or not treated with 100 μg/ml non-labeled siNPs for 24 h and incubated in complete DMEM medium and in serum-free starvation medium for 4 h in the presence or absence of bafilomycin A1 (100 nM). *Left*, live confocal images of the different treatments as indicated. *Right*, the number of yellow puncta (autophagosomes) and the number of RFP LC3-positive puncta (autolysosomes) in the merged images were counted, and the total number of puncta per cell was calculated as percentage. Data are presented as the mean ± S.E., *n* = 3 independent experiments; *, *p* < 0.05.

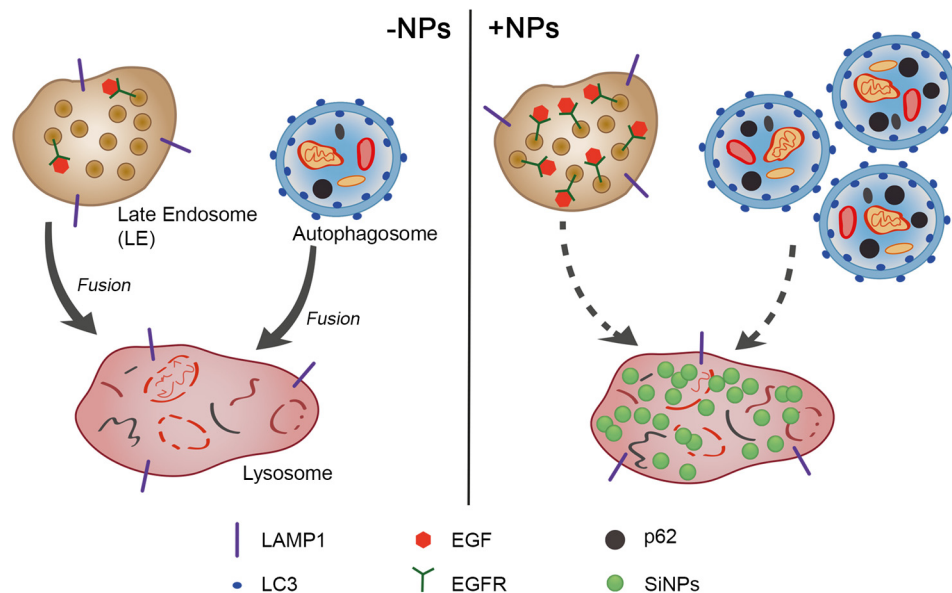


FIGURE 10. **Schematic model illustrating the effect of SiNPs on the endolysosomal system.** Under control conditions ($-SiNPs$, left), receptor-bound EGF is sorted into late endosomes (LE), which eventually fuse with lysosomes. LC3- and p62-containing autophagosomes also fuse with lysosomes for degradation. SiNP accumulation in lysosomes ($+SiNPs$, right) inhibits fusion of both late endosomes and autophagosomes with lysosomes, resulting in impaired degradation of EGF/EGFR and elevated levels of LC3- and p62-positive autophagosomes.

treated with siNPs for 24 h. Because of the fact that the GFP signal is quenched in acidic compartments, this probe makes it possible to differentiate between autophagosomes (GFP-positive and RFP-positive or yellow puncta) and autolysosomes (GFP-negative and RFP-positive or red puncta). Twenty cells were analyzed per assay in ImageJ.

SiNP Uptake, Immunocytochemistry, and Fluorescence Microscopy

HeLa cells grown on poly-(L-lysine)-coated glass coverslips were washed with PBS and incubated at 37 °C and 5% CO₂ for 4 h in DMEM (+10% FBS) supplemented with 20 $\mu\text{g ml}^{-1}$ SiNPs. After washing with PBS (+10 mM MgCl₂), cells were fixed with 4% paraformaldehyde for 10 min at room temperature, permeabilized, blocked in goat serum dilution buffer (30% goat serum, 0.1% Triton X-100 in sodium phosphate buffer, pH 7.4), and antibody-stained. Samples were imaged on a Zeiss Axiovert 200M-based spinning disk confocal microscope (PerkinElmer Life Sciences) under the control of Volocity (Improvision Inc.).

Antibodies; siRNAs

The following antibodies were used in this study: EEA1 (mouse, BD Transduction Laboratories), LAMP1 (mouse, clone CD107a/H4A3, Pharmingen), caveolin1 (mouse, BD Transduction Laboratories; and rabbit, Santa Cruz Biotechnology), clathrin (mouse, clone TD1; homemade antibody), flotillin1 (mouse, BD Transduction Laboratories), dynamin 1 + 2 (mouse, BD Biosciences), actin (mouse, clone ac15, Sigma), Hsp70 (mouse, Affinity BioReagents), mannose 6-phosphate receptor (mouse, CI-M6PR, Affinity BioReagents), CD63 (mouse, clone RFAC4, Millipore), AP-1 (mouse, 100/3, Sigma), LC3 for immunofluorescence (mouse, 4E10, MBL International) and for immunoblot (rabbit, Novus Biochemical), p62 (mouse, p62 lck ligand, BD Transduction Laboratories), pEGFR

(rabbit, D7A5, Cell Signaling), EGF receptor (EGFR) (rabbit, D38B1, Cell Signaling), pErk1/2 (mouse, clone MAPK-YT, Sigma), Erk1/2 (mouse, clone 9B3, Abcam), Oregon Green (rabbit, Invitrogen), ULK1 (rabbit, D8H5, Cell Signaling), phospho-ULK1 (Ser-757) (rabbit, Cell Signaling), p70 S6K (rabbit, 49D7, Cell Signaling), phospho-p70 S6K (Thr-389) (rabbit, 108D2, Cell Signaling). Secondary antibodies for immunofluorescence labeled with AlexaFluor dyes were all purchased from Invitrogen, and HRP-coupled antibodies for immunoblotting were from Dianova/Jackson ImmunoResearch.

The following siRNAs were used to knockdown protein expression: GUA ACU GUC GGC UCG UGG UTT (scrambled); CCU GAU UGA GAU UCA GUG C (caveolin 1 single siRNA); a) CUA AAC ACC UCA ACG AUG A, b) GCA AAU ACG UAG ACU CGG A, c) GCA GUU GUA CCA UGC AAU A, d) GCA UCA ACU UGC AGA AAG A (caveolin 1 smart-pool from Thermo Scientific); GCA ACU GAC CAA CCA CAU CTT (dynamin2); AUC CAA UUC GAA GAC CAA U (clathrin heavy chain) and CAC ACU GAC CCU CAA UGU C (flotillin 1).

Electron Microscopy

Glutaraldehyde-fixed HeLa cells treated with SiNPs were dehydrated and embedded in epoxy resin for subsequent electron microscopic analysis.

Autophagy Assays

Procedure for Fluorescence Microscopy—Cells were incubated with 20 $\mu\text{g ml}^{-1}$ and 100 $\mu\text{g ml}^{-1}$ SiNPs for 24 h. 4 h before incubation was stopped, serum-free medium was added together with 100 nM bafilomycin A1 (Sigma) to the corresponding samples. After washing with ice-cold PBS, cells were paraformaldehyde-fixed and processed for immunostaining with LC3. Digitonin (Invitrogen) was used to permeabilize the cells for LC3 staining. Images were taken with a confocal micro-

Nanoparticle-induced Lysosomal Dysfunction

scope LSM710 (Zeiss). Approximately 40 cells were analyzed per assay in ImageJ under identical threshold conditions.

Immunoblotting—After nanoparticle incubation (see above) cells were lysed on ice for 30–60 min in lysis buffer (2% Triton X-100, 20 mM HEPES, pH 7.4, 100 mM KCl, 4 mM MgCl₂, 1 mM PMSF, 0.03% protease inhibitor mixture (Sigma); PMSF and protease inhibitor mixture were added freshly). Crude cell lysates were analyzed by SDS-PAGE and immunoblotting. Band intensities were quantified using Fiji and Licor odyssey software.

Lysosomal pH Measurements

Lysosomal pH was determined by ratiometric fluorescence imaging using a pH-sensitive Oregon Green® 488 dye coupled to a 10-kDa dextran (OGD; Molecular Probes). A standard pulse-chase protocol was used to specifically target the fluorophore to lysosomes. Therefore, cells were grown on MatTek glass-bottom dishes to a confluence of 80%. The PBS-washed cells were treated with 20 μg of ml⁻¹ SiNPs (–FITC) for 4 h in DMEM (+10% FBS). After two additional PBS washing steps, 0.5 mg/ml OGD was loaded onto the cells and incubated overnight in DMEM (+10% FBS). The next day cells were washed with PBS, and the pH-sensitive dye was chased into lysosomes for 2 h at 37 °C in DMEM (+10% FBS). Control experiments were conducted to prove the localization of Oregon Green to LAMP1- and CD63-positive structures. The fluorophore was excited at a wavelength of 440 and 488 nm, respectively, and ratiometric fluorescence images were acquired with an inverted microscope (Zeiss Axiovert 200 equipped with a 100 × 1.30 NA oil immersion objective) connected to a Polychrom II monochromator (TILL photonics). After passing a 535 ± 20-nm filter, the emitted light was captured with a Sencicam CCD camera (PCO Inc., Kelheim, Germany). For each sample (control and +NPs) at least 10 different cells were measured in imaging solution (10 mM glucose, 2 mM CaCl₂, 1 mM MgCl₂, 135 mM NaCl, 5 mM KCl, 10 mM HEPES, pH 7.4). Image analysis was performed using a self-programmed Macro for Fiji ImageJ. Therefore, regions of interest (ROIs) were defined as areas above a certain fluorescence threshold in the acquired images at 488-nm excitation to then calculate the ratio of the mean intensity of the 488 and the 440 channel for each ROI. To finally evaluate the pH for each measurement, an *in situ* pH calibration was conducted at the end of each experiment by treating the cells with isotonic K⁺-based solutions (5 mM NaCl, 1 mM CaCl₂, 115 mM KCl, 1.2 mM MgSO₄, 10 mM glucose, 25 mM of either HEPES, MES, or potassium acetate) ranging in pH from 3.5 to 7.0 and supplemented with 10 μM concentrations of both nigericin (Tocris Bioscience) and monensin (Sigma). The resulting fluorescence intensity ratio (488 nm/440 nm) was fitted with a sigmoidal function and used to interpolate the pH value from the experimental ratio data.

Analysis of Cell Viability and Cytotoxicity

MTT Assay to Measure Metabolic Activity—HeLa cells were seeded in 96-well plates at a density of 10,000 cells per well. The next day cells were incubated for 24 h with different concentrations of SiNPs (±FITC). Afterward, cells were washed twice with PBS. The addition of MTT (3-[4,5-dimethylthiazol-2-yl]

2,5-diphenyl-tetrazolium bromide), and following procedure was carried out according to manufacturer's instructions (Invitrogen). The absorbance was measured at 562 nm with a Safire2 plate reader (Tecan AG).

TUNEL Apoptosis Assay—Apoptosis was assayed by the TUNEL Apoptosis Detection kit (Invitrogen Click-iTunel AlexaFluor 647 Imaging Assay) according to the provided manual. Briefly, HeLa cells were seeded in 96-well plates. Asynchronously growing cells were treated in the presence or absence of SiNPs at the indicated concentration for 24 h. Cells were washed, fixed with 4% paraformaldehyde, permeabilized in PBS, 0.25% Triton X-100, and processed for TUNEL staining according to the manufacturer's protocol. Cells treated with DNase I for 15 min served as a positive control. Samples were analyzed by epifluorescence microscopy and quantified.

Lactate Dehydrogenase Activity-based Necrosis Assay—Toxicity due to membrane permeabilization (necrosis) was assayed by determination of lactate dehydrogenase activity using the TaKaRa LDH Cytotoxicity Kit. HeLa cells were seeded in 96-well plates. Asynchronously growing cells were treated in the presence or absence of SiNPs at the indicated concentration for 24 h. The supernatant (100 μl) was incubated with lactate dehydrogenase assay reagent according to the manufacturer's protocol and measured at 490 nm (plate background absorbance) using Tecan Safire plate reader. Values were normalized to drug/media background value, and toxicity was calculated as a % of a 100% Triton X-100-lysed cell control (100% necrosis).

EGFR Signaling—HeLa cells at a confluence of 90% were incubated with 20 μg/ml SiNPs for 4 h, then washed and starved in DMEM for 2 h. The samples were then stimulated for 0 and 30 min with 500 ng/ml unlabeled EGF in DMEM supplemented with 10 μg/ml cycloheximide. Subsequently cells were washed and lysed (1% Triton X-100, 20 mM HEPES pH 7.4, 100 mM KCl, 2 mM MgCl₂, 1 mM PMSF, 0.03% protease inhibitor mixture (Sigma); PMSF and protease inhibitor mixture were added freshly). Phosphatase inhibitor mixture (Sigma) was added for the analysis of phosphorylated proteins. Lysates were spun at 20,000 × g for 10 min to get rid of cell nuclei, and debris and supernatants were then analyzed by SDS/PAGE and immunoblotting.

EGF Degradation Assay—After SiNPs incubation (as described above), cells were washed three times with PBS and then conducted to starvation for 2 h in DMEM followed by incubation with 100 ng/ml EGF-Alexa647 (Molecular Probes) for 30 min on ice. Cells were then washed 2 times with ice-cold PBS and incubated in DMEM for 30, 60, and 120 min at 37 °C. Immediately afterward, cells were washed on ice and processed for immunocytochemistry. To evaluate EGFR levels, coverslips were paraformaldehyde fixed right after the 30 min on ice incubation with EGF-Alexa647.

Transferrin Recycling Assay—After incubation with SiNPs, cells were washed 3 times with PBS and then starved for 1 h in DMEM followed by incubation with 20 μg/ml Tf-Alexa647 (Molecular Probes) for 30 min on ice. Subsequently cells were washed 2 times with ice-cold PBS and incubated in DMEM for 5, 15, and 60 min at 37 °C. Immediately afterward, cells were washed on ice and processed for immunocytochemistry. To evaluate transferrin (Tf) receptor levels, coverslips were para-

formaldehyde-fixed right after the 30 min on ice incubation with Tf-Alexa647.

LysoTracker—Cells were grown overnight on coverslips, washed once with PBS, and incubated with 20 $\mu\text{g}/\text{ml}$ SiNPs in DMEM (+10% FBS) supplemented with 50 nM LysoTracker[®] Red DND-99 (Invitrogen) for 4 h at 37 °C. Afterward cells were washed thoroughly with PBS and imaged live in HBSS, 10 mM HEPES at 37 °C and 5% CO₂.

Cathepsin B/L Lysosomal Protease Activity—Cells were seeded on MatTek glass-bottom dishes (MatTek Corp.) and cultured overnight at 37 °C and 5% CO₂. Washed cells were then incubated with 20 $\mu\text{g}/\text{ml}$ SiNPs in DMEM (+10% FBS) for 4 h, washed thoroughly, and subsequently treated according to the manufacturer's protocol. The total incubation time with Magic RedTM Cathepsin B/L (both from Immunochemistry Technologies) was 60 min at 37 °C and 5% CO₂. Hoechst was added directly to cells 15 min before imaging.

Data Analysis and Statistics—Data are expressed as the means \pm S.E. of at least three experiments. The statistical significance was assessed by using the unpaired *t* test.

Author Contributions—Q. G., D. N., M. S., and C. M. G. synthesized and characterized SiNPs, I. S. and T. L.-H. carried out all cell biological and biochemical experiments, S. J. aided with lysosomal pH measurements, D. P. carried out electron microscopic analyses of cells, and V. H. together with E. R. and C. M. G. conceived the study, supervised, and coordinated the experiments and wrote the manuscript with input from all authors.

Acknowledgments—We thank Uwe Fink (Leibniz-Institut für Molekulare Pharmakologie, Berlin) for help with the cell viability assays, Dr. Nils Bohmer (MagForce AG, Berlin) for the kind gift of iron oxide nanoparticles, and Dr. H. Renz and Prof. Dr. R. J. Radlanski (Department of Craniofacial Developmental Biology, Charité Berlin, Germany) for use of their electron microscope.

References

- Cheng, Z., Al Zaki, A., Hui, J. Z., Muzykantov, V. R., and Tsourkas, A. (2012) Multifunctional nanoparticles: cost versus benefit of adding targeting and imaging capabilities. *Science* **338**, 903–910
- Sengupta, S., Eavarone, D., Capila, I., Zhao, G., Watson, N., Kiziltepe, T., and Sasisekharan, R. (2005) Temporal targeting of tumour cells and neovasculature with a nanoscale delivery system. *Nature* **436**, 568–572
- Hirsch, L. R., Stafford, R. J., Bankson, J. A., Sershen, S. R., Rivera, B., Price, R. E., Hazle, J. D., Halas, N. J., and West, J. L. (2003) Nanoshell-mediated near-infrared thermal therapy of tumors under magnetic resonance guidance. *Proc. Natl. Acad. Sci. U.S.A.* **100**, 13549–13554
- Santra, S., Zhang, P., Wang, K., Tapeç, R., and Tan, W. (2001) Conjugation of biomolecules with luminophore-doped silica nanoparticles for photo-stable biomarkers. *Anal. Chem.* **73**, 4988–4993
- Zhang, F. F., Wan, Q., Li, C. X., Wang, X. L., Zhu, Z. Q., Xian, Y. Z., Jin, L. T., and Yamamoto, K. (2004) Simultaneous assay of glucose, lactate, L-glutamate and hypoxanthine levels in a rat striatum using enzyme electrodes based on neutral red-doped silica nanoparticles. *Anal. Bioanal. Chem.* **380**, 637–642
- Slowing, I. I., Vivero-Escoto, J. L., Wu, C. W., and Lin, V. S. (2008) Mesoporous silica nanoparticles as controlled release drug delivery and gene transfection carriers. *Adv. Drug. Deliv. Rev.* **60**, 1278–1288
- Nel, A., Xia, T., Mädler, L., and Li, N. (2006) Toxic potential of materials at the nanolevel. *Science* **311**, 622–627
- Halamoda Kenzaoui, B., Chapuis Bernasconi, C., Guney-Ayra, S., and Juillerat-Jeanerret, L. (2012) Induction of oxidative stress, lysosome activation and autophagy by nanoparticles in human brain-derived endothelial cells. *Biochem. J.* **441**, 813–821
- Xia, T., Kovochich, M., Brant, J., Hotze, M., Sempf, J., Oberley, T., Sioutas, C., Yeh, J. I., Wiesner, M. R., and Nel, A. E. (2006) Comparison of the abilities of ambient and manufactured nanoparticles to induce cellular toxicity according to an oxidative stress paradigm. *Nano Lett.* **6**, 1794–1807
- Ma, N., Ma, C., Li, C., Wang, T., Tang, Y., Wang, H., Moul, X., Chen, Z., and Hel, N. (2013) Influence of nanoparticle shape, size, and surface functionalization on cellular uptake. *J. Nanosci. Nanotechnol.* **13**, 6485–6498
- Treuel, L., Jiang, X., and Nienhaus, G. U. (2013) New views on cellular uptake and trafficking of manufactured nanoparticles. *J. R. Soc. Interface* **10**, 20120939
- Fisichella, M., Dabboue, H., Bhattacharyya, S., Lelong, G., Saboungi, M. L., Warmont, F., Midoux, P., Pichon, C., Guérin, M., Hevor, T., and Salvétat, J. P. (2010) Uptake of functionalized mesoporous silica nanoparticles by human cancer cells. *J. Nanosci. Nanotechnol.* **10**, 2314–2324
- Doherty, G. J., and McMahon, H. T. (2009) Mechanisms of endocytosis. *Annu. Rev. Biochem.* **78**, 857–902
- Howes, M. T., Mayor, S., and Parton, R. G. (2010) Molecules, mechanisms, and cellular roles of clathrin-independent endocytosis. *Curr. Opin. Cell Biol.* **22**, 519–527
- von Kleist, L., and Haucke, V. (2012) At the crossroads of chemistry and cell biology: inhibiting membrane traffic by small molecules. *Traffic* **13**, 495–504
- Cleal, K., He, L., Watson, P. D., and Jones, A. T. (2013) Endocytosis, intracellular traffic and fate of cell penetrating peptide based conjugates and nanoparticles. *Curr. Pharm. Des.* **19**, 2878–2894
- Settembre, C., Fraldi, A., Medina, D. L., and Ballabio, A. (2013) Signals from the lysosome: a control centre for cellular clearance and energy metabolism. *Nat. Rev. Mol. Cell Biol.* **14**, 283–296
- Raiborg, C., and Stenmark, H. (2009) The ESCRT machinery in endosomal sorting of ubiquitylated membrane proteins. *Nature* **458**, 445–452
- Luzio, J. P., Gray, S. R., and Bright, N. A. (2010) Endosome-lysosome fusion. *Biochem. Soc. Trans.* **38**, 1413–1416
- Arriagada, F. J., and Osseo-Asare, K. (1999) Synthesis of nanosize silica in a nonionic water-in-oil microemulsion: effects of the water/surfactant molar ratio and ammonia concentration. *J. Colloid Interface Sci.* **211**, 210–220
- Stöber, W., Fink, A., and Bohn, E. (1968) Controlled growth of monodisperse silica spheres in micron size range. *J. Colloid Interface Sci.* **26**, 62–69
- Graf, C., Gao, Q., Schütz, I., Noufele, C. N., Ruan, W., Posselt, U., Korotianskiy, E., Nordmeyer, D., Rancan, F., Hadam, S., Vogt, A., Lademann, J., Haucke, V., and Rühl, E. (2012) Surface functionalization of silica nanoparticles supports colloidal stability in physiological media and facilitates internalization in cells. *Langmuir* **28**, 7598–7613
- Glebov, O. O., Bright, N. A., and Nichols, B. J. (2006) Flotillin-1 defines a clathrin-independent endocytic pathway in mammalian cells. *Nat. Cell Biol.* **8**, 46–54
- Howes, M. T., Kirkham, M., Riches, J., Cortese, K., Walsler, P. J., Simpson, F., Hill, M. M., Jones, A., Lundmark, R., Lindsay, M. R., Hernandez-Deviez, D. J., Hadzic, G., McCluskey, A., Bashir, R., Liu, L., Pilch, P., McMahon, H., Robinson, P. J., Hancock, J. F., Mayor, S., and Parton, R. G. (2010) Clathrin-independent carriers form a high capacity endocytic sorting system at the leading edge of migrating cells. *J. Cell Biol.* **190**, 675–691
- Henley, J. R., Krueger, E. W., Oswald, B. J., and McNiven, M. A. (1998) Dynamin-mediated internalization of caveolae. *J. Cell Biol.* **141**, 85–99
- Schwake, M., Schröder, B., and Saftig, P. (2013) Lysosomal membrane proteins and their central role in physiology. *Traffic* **14**, 739–748
- Al-Rawi, M., Diabaté, S., and Weiss, C. (2011) Uptake and intracellular localization of submicron and nano-sized SiO₂ particles in HeLa cells. *Arch. Toxicol.* **85**, 813–826
- Liang, H., Jin, C., Tang, Y., Wang, F., Ma, C., and Yang, Y. (2014) Cytotoxicity of silica nanoparticles on HaCaT cells. *J. Appl. Toxicol.* **34**, 367–372
- Mizushima, N., and Komatsu, M. (2011) Autophagy: renovation of cells and tissues. *Cell* **147**, 728–741

Nanoparticle-induced Lysosomal Dysfunction

30. Weinert, S., Jabs, S., Supanchart, C., Schweizer, M., Gimber, N., Richter, M., Rademann, J., Stauber, T., Kornak, U., and Jentsch, T. J. (2010) Lysosomal pathology and osteopetrosis upon loss of H⁺-driven lysosomal Cl-accumulation. *Science* **328**, 1401–1403
31. Chaudhary, N., Gomez, G. A., Howes, M. T., Lo, H. P., McMahon, K. A., Rae, J. A., Schieber, N. L., Hill, M. M., Gaus, K., Yap, A. S., and Parton, R. G. (2014) Endocytic crosstalk: cavins, caveolins, and caveolae regulate clathrin-independent endocytosis. *PLoS Biol.* **12**, e1001832
32. Sandhoff, K., and Harzer, K. (2013) Gangliosides and gangliosidoses: principles of molecular and metabolic pathogenesis. *J. Neurosci.* **33**, 10195–10208
33. Moreau, K., Renna, M., and Rubinsztein, D. C. (2013) Connections between SNAREs and autophagy. *Trends Biochem. Sci.* **38**, 57–63
34. Pinot, M., Vanni, S., Pagnotta, S., Lacas-Gervais, S., Payet, L. A., Ferreira, T., Gautier, R., Goud, B., Antonny, B., and Barelli, H. (2014) Lipid cell biology: polyunsaturated phospholipids facilitate membrane deformation and fission by endocytic proteins. *Science* **345**, 693–697
35. Nixon, R. A. (2013) The role of autophagy in neurodegenerative disease. *Nat. Med.* **19**, 983–997

Lysosomal Dysfunction Caused by Cellular Accumulation of Silica Nanoparticles

Irene Schütz, Tania Lopez-Hernandez, Qi Gao, Dmytro Puchkov, Sabrina Jabs, Daniel Nordmeyer, Madlen Schmutde, Eckart Rühl, Christina M. Graf and Volker Haucke

J. Biol. Chem. 2016, 291:14170-14184.

doi: 10.1074/jbc.M115.710947 originally published online May 11, 2016

Access the most updated version of this article at doi: [10.1074/jbc.M115.710947](https://doi.org/10.1074/jbc.M115.710947)

Alerts:

- [When this article is cited](#)
- [When a correction for this article is posted](#)

[Click here](#) to choose from all of JBC's e-mail alerts

This article cites 35 references, 11 of which can be accessed free at <http://www.jbc.org/content/291/27/14170.full.html#ref-list-1>